Band alignment at surfaces and heterointerfaces of Al_2O_3, Ga_2O_3, In_2O_3, and related group-III oxide polymorphs: A first-principles study

Yoyo Hinuma,[1,2,*] Tomoya Gake,[3] and Fumiyasu Oba[3,2,†]

[1]*Center for Frontier Science, Chiba University, Chiba 263-8522, Japan*

[2]*Center for Materials Research by Information Integration, Research and Services Division of Materials Data and Integrated System, National Institute for Materials Science, Tsukuba 305-0047, Japan*

[3]*Laboratory for Materials and Structures, Institute of Innovative Research, Tokyo Institute of Technology, Yokohama 226-8503, Japan*

(Received 25 June 2019; revised manuscript received 2 August 2019; published 23 August 2019)

The band alignments at nonpolar surfaces and heterointerfaces of Al_2O_3, Ga_2O_3, and In_2O_3 polymorphs, and three related group-III oxides, namely, Sc_2O_3, Y_2O_3, and La_2O_3, are investigated by using first-principles calculations. A non-self-consistent dielectric-dependent hybrid functional approach is adopted on top of semilocal density-functional calculations by using the Perdew-Burke-Ernzerhof functional tuned for solids (PBEsol) to accelerate the band alignment evaluation that involves surface and interface calculations. Among the five crystal structures considered, namely, corundum, β-gallia, κ-alumina, bixbyite (C-type rare earth), and A-type rare earth, the lowest energy phases are corundum, β-gallia, A-type rare earth, and bixbyite for Al_2O_3, Ga_2O_3, La_2O_3, and the others, respectively, within PBEsol calculations. The ionization potential typically decreases in the order Al_2O_3, Ga_2O_3, In_2O_3, Sc_2O_3, Y_2O_3, and La_2O_3 within the same crystal structure and surface termination. This tendency is enhanced by the atomic relaxation-induced surface dipoles, where smaller cations tend to relax toward the bulk side compared to O ions, while larger cations tend to relax toward the vacuum side. The ionization potential and electron affinity differences at unrelaxed surfaces are good indicators of the interfacial valence- and conduction-band offsets, respectively, for Al_2O_3/Ga_2O_3 with a relatively small mismatch in the lattice parameters of the two phases.

DOI: 10.1103/PhysRevMaterials.3.084605

I. INTRODUCTION

Oxides of group-IIIB elements have a variety of important applications. Corundum structure Al_2O_3, or α-Al_2O_3, is used as substrates for GaN-based light-emitting diodes [1], optical waveguides [2], gate insulators [3], oxidation and corrosion protective scales [4], thermal barrier coatings [5], tritium permeation barriers in future fusion reactors [6], and so forth. The θ-Al_2O_3 phase is isostructural with the monoclinic β-gallia structure and is used as the Pt atom support in CO [7] and NO [8] oxidation catalysts. The β phase of Ga_2O_3 has been considered as an n-type wide-gap semiconductor for solar-blind UV detectors [9,10], gas sensors [11], and transparent conductors [12,13]. Recently, its high Johnson's (power-frequency capability) and Baliga's (specific on-resistance in vertical drift region) figures of merit, as well as relatively cost-effective device fabrication, have been attracting significant research interest in power device applications [14,15]. In addition to the β phase, at least four polymorphs of Ga_2O_3 are known, which are rhombohedral α- (corundum structure), cubic γ- (defective spinel structure), cubic δ- (bixbyite structure, which is also denoted as the C-type rare-earth structure), and orthorhombic ε-Ga_2O_3 isomorphic to κ-Al_2O_3. Sometimes a disordered structure with $P6_3mc$ space-group symmetry is labeled as ε-Ga_2O_3, which is comprised of domains of an ordered phase labeled κ-Ga_2O_3 that is the same as the ordered orthorhombic ε-Ga_2O_3 with $Pna2_1$ space-group symmetry [16]. These four phases are considered metastable [17,18], but the α- [19,20], γ- [21–23], and ε-Ga_2O_3 [24–26] phases can be grown on various kinds of substrates. In particular, α-Ga_2O_3 has been studied as a wide-gap semiconductor. Examples are n-type doping with Sn [27] in a manner similar to the β phase [28] and alloying with isostructural α-Al_2O_3 for band-gap engineering [29–31]. In_2O_3 typically crystalizes in the bixbyite structure. Heavily doped n-type In_2O_3, where Sn is commonly used as the dopant, is a prototypical transparent conductive oxide for electrode applications [32–34].

Many applications of these group-IIIB oxides are governed by their surfaces or heterointerfaces, where not only the band gaps but also the valence- and conduction-band positions against the vacuum level or the bands of other materials are key fundamental quantities. The band alignment that systematically maps the relative band positions serves as the foundation of such surface and heterointerface design [35–39]. Evaluation of the surface band alignment can be made by comparing the valence-band maximum (VBM) and the conduction-band minimum (CBM) against the vacuum level or, in other words, the ionization potential (IP) and electron affinity (EA). IPs and EAs also often provide reasonable estimates of heterojunction band offsets, especially when the constituent materials of an interface have similar crystal and electronic structures and/or charge transfer across the interface is not significant [38,40–44]. Here, it should be noted that the IPs and EAs are surface-dependent quantities and are

*yoyo.hinuma@gmail.com
†oba@msl.titech.ac.jp

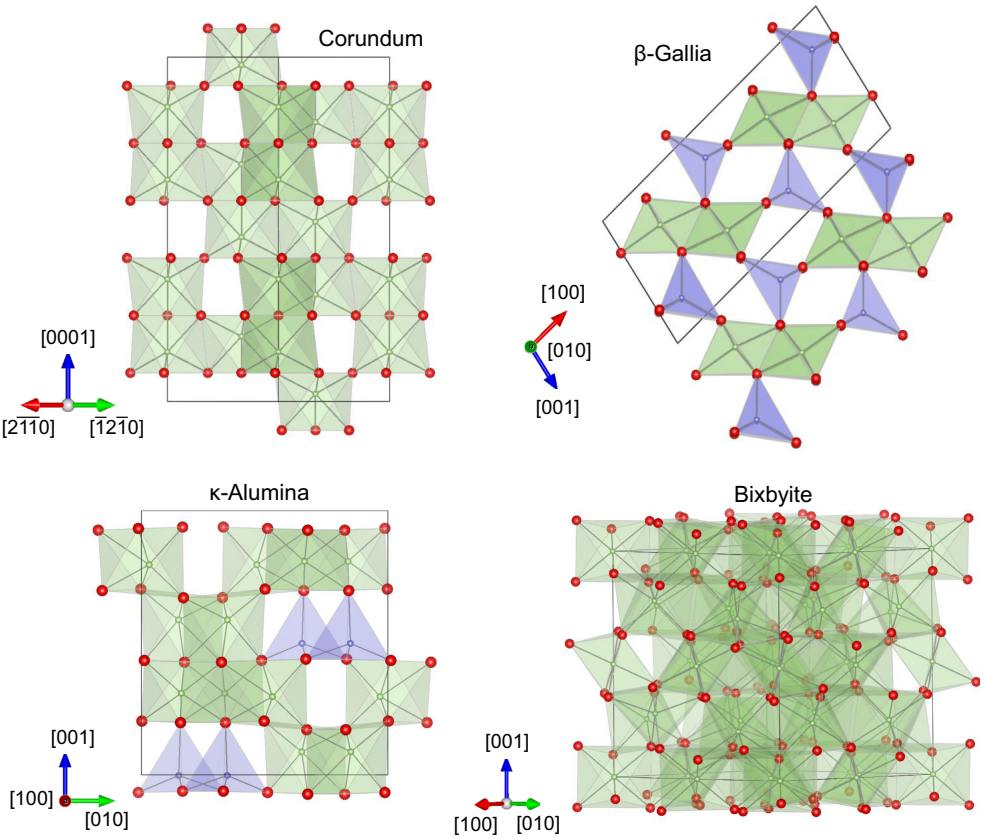

FIG. 1. Crystal structures of group-III oxides considered for band alignment evaluation. Sixfold and fourfold coordinated cations are shown in green and blue polyhedra, respectively, while O ions are shown as red balls.

affected by the surface dipole contribution, which depends on the orientation, atomic structure, composition, and adsorption at the surfaces [35,45,46]. Therefore, knowing the possible magnitude of discrepancy between the IP (or EA) difference and the heterojunction band offset over an explicit interface is important when interfacial band offsets are of interest. For instance, the differences between natural valence-band offsets and IP differences for the (110) interfaces and surfaces of chalcopyrite $CuGaSe_2$, $CuInSe_2$, $ZnSnP_2$, or $CdSnP_2$ and zincblende ZnS or CdS have been reported to be at most ∼0.2 eV [41]. The small differences can be justified by the fact that the materials on both sides of the interface share the same framework and the surface orientation and termination are of Tasker's type 1 [47], which means that all layers are stoichiometric and nonpolar. However, a more systematic study of the (110) interfaces of 17 group-IV, III-V, and II-VI semiconductors shows that the maximum deviation could be as large as 0.85 eV in antimonides [40] even though the surface termination and orientation are of Tasker's type 1.

This study investigates the band alignment of four polymorphs, which are corundum, β-gallia, κ-alumina, and bixbyite (C-type rare earth; Fig. 1), for Al_2O_3, Ga_2O_3, and In_2O_3 by using first-principles calculations. The effect of crystal structure is of interest, particularly for Al_2O_3 and Ga_2O_3 that exhibit various polymorphs, as mentioned above. Relevant group-IIIA oxides such as Sc_2O_3, Y_2O_3, and La_2O_3 are also included in the target systems to discuss trends from a wider perspective. We first examine the relative stability of the polymorphs. The A-type rare-earth structure was also considered here because La_2O_3 is known to take this structure. Dielectric-dependent (dd) hybrid functional calculations based on a non-self-consistent (nsc) approach are then used for the evaluation of the band positions at their nonpolar surfaces and heterointerfaces with various orientations and terminations; nsc calculations have been shown to yield band structures and surface band positions similar to self-consistent solutions for a number of semiconductors and insulators while substantially reducing computational costs [48–51]. The discrepancy in the band alignment between approaches with and without the use of an explicit interface model is discussed for Al_2O_3/Ga_2O_3 interfaces, as well as the trends of the surface and interface band positions with respect to the chemical composition, crystal structure, and surface or interface orientation.

II. METHODOLOGY

A. Computational procedures

First-principles calculations were conducted by using the projector augmented-wave method [52], as implemented in the VASP code [53,54]. The Perdew-Burke-Ernzerhof functional tuned for solids (PBEsol) [55] within the generalized gradient approximation (GGA) was used for total energy evaluation and geometry optimization because it provides reasonable bulk energetics and crystal structures; for instance, compared with the standard PBE-GGA functional [56], as

shown in our previous systematic study of group-I to VI binary oxides [57]. For the discussion of the relative stability of the polymorphs, the PBE-GGA, the strongly constrained and appropriately normed (SCAN) meta-GGA [58], and Heyd-Scuseria-Ernzerhof (HSE06) range-separated hybrid [59–61] functionals were adopted in addition to PBEsol. The nsc-dd hybrid functional calculation formalism was employed to enable sufficiently accurate and efficient evaluation of IPs and EAs [51,62]. In short, the reciprocal of the average of the trace of the static electronic dielectric tensor was used as the nonlocal Fock-exchange mixing parameter in the full-range hybrid functional [50,63–70], where the exchange-correlation was otherwise treated by using PBEsol. The dielectric tensors were calculated by using PBEsol and the random-phase approximation (RPA) based on density-functional perturbation theory [71,72]. These dd hybrid functional calculations were performed non-self-consistently by using PBEsol wave functions and charge density. Bulk eigenvalues from nsc-dd hybrid functional calculations can then be aligned with the results of PBEsol surface and interface calculations by using the common electrostatic potential reference. This allows us to obtain IPs, EAs, and interfacial band offsets approximately at the dd hybrid functional level without computationally demanding hybrid functional calculations for surfaces and interfaces; our previous work on group-IV, III-V, and II-VI semiconductors showed that the difference in the band gap between nsc and sc HSE06 calculations is ∼0.1 eV or less, and the difference in the IP and EA is typically ∼0.1 eV but is ∼0.4 eV in MgO and ZnO [62]. We expect errors of a similar magnitude associated with self-consistency in the nsc-dd hybrid calculations. Still, the resultant band positions, as well as band gaps, are in reasonable agreement with experimental values, as will be discussed later for group-III oxides and have been shown previously for prototypical semiconductors [62] and group-II oxides [51].

Bulk geometry optimization was conducted by using a plane-wave basis set with an energy cutoff of 550 eV and even k-point meshes that were determined on the basis of convergence of total energies: the criterion of the total energy change was set at 0.005 meV per atom per the number of incremental k points starting from the k-point density higher than 0.06 Å^{-1} in the crystallographer's definition along each reciprocal basis vector [57,74]. Slab-and-vacuum models for nonpolar surfaces, where slabs infinitely extending in two directions (in-plane directions) are alternated with a vacuum region in the other direction under three-dimensional periodic boundary conditions, were constructed based on the algorithm by Hinuma *et al.* [51,75]. Slabs with thickness larger than 15 Å and vacuum thickness larger than 12 Å were used for a high level of convergence. The slab thickness was checked for surfaces of corundum and β-gallia structures, which have relatively small unit cells, based on the process in our previous work [51]. The average local potential at atomic sites at the center one-third of the slab, whose thickness is defined as the distance between the outermost atoms, was used as an electrostatic reference level for the alignment between the bulk, surface, and interface models in the evaluation of IP, EA, and interfacial band offsets. Heterostructure supercells to model heterointerfaces were constructed based on a multiple of three repeat units of each component material, where the average local potential at the center one-third atomic sites in each layer was used as the electrostatic reference.

B. Derivation of band alignment

One way to construct the band alignment is to use the IPs and EAs at surfaces, which are pertinent to the design and prediction of surface properties. Section III first discusses such surface-based band alignments and then examines band offsets over heterointerfaces. Three categories of calculations appear in the interfacial band offset derivation between phases A and B. In the case of the valence-band offset, they are (1) a bulk nsc-dd hybrid functional calculation of a single phase A (or B) that is used to obtain the energy difference between the VBM and a reference level, which is denoted as $\Delta\varepsilon^{\mathrm{A}}_{\mathrm{VBM-Ref}}$ (or $\Delta\varepsilon^{\mathrm{B}}_{\mathrm{VBM-Ref}}$); (2) a surface calculation of a single phase A (or B) using PBEsol to evaluate the energy difference between the vacuum level and a reference level, defined as $\Delta\varepsilon^{\mathrm{A}}_{\mathrm{Vac-Ref}}$ (or $\Delta\varepsilon^{\mathrm{B}}_{\mathrm{Vac-Ref}}$); and (3) an interface calculation using PBEsol to assess the difference between reference levels in a model containing an explicit interface between two phases A and B, which is $\Delta\varepsilon^{\mathrm{A-B}}_{\mathrm{Ref}}$.

The differences between natural (unstrained) valence-band offset estimated with or without an interface model and with or without relaxation are also discussed. The natural valence-band offset between phases A and B obtained with an interface model is defined as

$$\begin{aligned}\Delta\varepsilon^{\mathrm{A-B}}_{\mathrm{Interface,Natural,IC}} &= \left(\Delta\varepsilon^{\mathrm{A}}_{\mathrm{VBM-Ref,Natural,Bulk}} - \Delta\varepsilon^{\mathrm{A}}_{\mathrm{Vac-Ref,Natural,IC}} + \Delta\varepsilon^{\mathrm{A}}_{\mathrm{Vac-Ref,Strained,IC}}\right) + \Delta\varepsilon^{\mathrm{A-B}}_{\mathrm{Ref,Strained,Interface}} \\ &\quad - \left(\Delta\varepsilon^{\mathrm{B}}_{\mathrm{VBM-Ref,Natural,Bulk}} - \Delta\varepsilon^{\mathrm{B}}_{\mathrm{Vac-Ref,Natural,IC}} + \Delta\varepsilon^{\mathrm{B}}_{\mathrm{Vac-Ref,Strained,IC}}\right), \end{aligned} \quad (1)$$

where the subscripts "Natural" and "Strained" indicate whether the in-plane lattice parameters are those of unstrained (natural) bulk or those of the interface model, respectively. The in-plane lattice parameters must be the same between two phases in the interface model and therefore strained. The lattice parameters and internal coordinates are fully relaxed in the interface calculations. The reference levels of surfaces with natural and strained in-plane lattice parameters

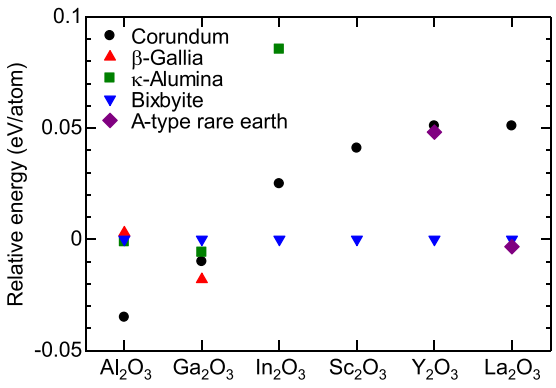

FIG. 2. Relative energies versus the bixbyite structure of five polymorphs obtained using PBEsol.

TABLE I. Relative energies of Ga_2O_3 polymorphs compared to the β-gallia structure based on different approximations. Units are in meV/atom.

Phase	PBEsol	PBE	SCAN	HSE06
α (corundum)	9	28	10	29
β (β-gallia)	0	0	0	0
ε (κ-alumina)	13	20	15	20
δ (bixbyite)	18	31	25	41

are aligned at the vacuum level in the surface slab-model calculations. "IC" indicates the choice of internal coordinates in the slab calculations. Possible choices are the relaxation of all internal coordinates in the surface calculations ("Relaxed") and fixing to those cleaved from perfect bulk ("Bulk"). For surfaces with strained in-plane lattice parameters with "Bulk" internal coordinates, the out-of-plane supercell dimensions were scaled such that the volume per atom is kept constant after changing the in-plane lattice parameters from natural to strained values. Conduction-band offsets can be obtained in a similar manner by considering the CBM instead of the VBM. Further detailed procedures are outlined in Ref. [41].

The IPs and EAs could also be used to estimate interfacial band offsets if the so-called electron affinity rule holds well [38,43,44]. For instance, the natural valence-band offset may be estimated by using IP differences at surfaces as

$$\begin{aligned}\Delta\varepsilon^{\mathrm{A-B}}_{\mathrm{Surface,Natural,IC}} &= \left(\Delta\varepsilon^{\mathrm{A}}_{\mathrm{VBM-Ref,Natural,Bulk}} - \Delta\varepsilon^{\mathrm{A}}_{\mathrm{Vac-Ref,Natural,IC}}\right) \\ &\quad - \left(\Delta\varepsilon^{\mathrm{B}}_{\mathrm{VBM-Ref,Natural,Bulk}} - \Delta\varepsilon^{\mathrm{B}}_{\mathrm{Vac-Ref,Natural,IC}}\right). \quad (2)\end{aligned}$$

Here, surface band positions without considering surface atomic relaxation would be suited as atomic relaxation at the interfaces is restricted by the presence of the counterpart material to some or large extent. We therefore consider band positions with fixed internal coordinates as well as relaxed cases for comparison.

III. RESULTS AND DISCUSSION

A. Relative stability and electronic properties of polymorphs

Figure 2 shows the relative energies between five crystal structures, which are corundum, β-gallia, κ-alumina, bixbyite (C-type rare earth), and A-type rare earth (space-group types $R\bar{3}c$, $C2/m$, $Pna2_1$, $Ia\bar{3}$, and $P\bar{3}m1$; space-group numbers 167, 12, 33, 206, and 164, respectively), of Al_2O_3, Ga_2O_3, In_2O_3, Sc_2O_3, Y_2O_3, and La_2O_3. The crystal structure cannot be sustained (lattice deformation index $LR_2 > 0.2$ and/or internal coordination relaxation index $CR > 0.25$ Å; the definitions are found in Ref. [57]) in In_2O_3, Sc_2O_3, Y_2O_3, and La_2O_3 for β-gallia; Sc_2O_3, Y_2O_3, and La_2O_3 for κ-alumina; and Al_2O_3 and Ga_2O_3 for A-type rare earth. Therefore, the corresponding values are not shown, as well as the values for other phases showing relative energies higher than 0.1 eV/atom. The bixbyite phases exhibit the lowest energies among the five crystal structures considered except for Al_2O_3, Ga_2O_3, and La_2O_3, where the lowest-energy structures are corundum, β-gallia, and A-type rare earth, respectively. The proportion of fourfold coordinated cations is 0%, 50%, 25%, 0%, and 0% in corundum, β-gallia, κ-alumina, bixbyite, and A-type rare earth, respectively; the rest of the cations are coordinated by six anions except for the A-type rare-earth structure that has only sevenfold coordinated cations. Therefore, the relative stability of these polymorphs implies that Al^{3+} and Ga^{3+} have some tolerance to the fourfold coordination while the other cations do not, which is consistent with a common chemical picture. Hereafter, the polymorphs other than A-type rare earth are considered because our primary focus is on Al_2O_3, Ga_2O_3, and In_2O_3.

The relative energy differences between α- (corundum), β-, δ- (bixbyite), and ε- (κ-alumina) Ga_2O_3 based on PBEsol, PBE, SCAN, and HSE are compared in Table I. The order of formation energies is β (most stable) $< \alpha < \varepsilon < \delta$ (least stable) in both PBEsol and SCAN, while PBE shows a different order of $\beta < \varepsilon < \alpha < \delta$, as found in a previous study [17]. The relative stability of HSE06 is the same order as in PBE. The energy differences between the Ga_2O_3 polymorphs are small in all of the considered functionals. Such energetic competition would explain why various polymorphs can be relatively easily obtained for Ga_2O_3 although accurate theoretical prediction of the relative stability is challenging. In addition, vibrational contributions to the free energy have been reported to affect the relative stability of Ga_2O_3 polymorphs at high temperatures [17].

The (averaged) static electronic dielectric constants obtained by using PBEsol and the RPA are listed in Table II and compared with available experimental values. The theoretical values are reasonably close to the corresponding experimental values. This can be attributed to the cancelation of errors associated with the underestimation of the band gaps and neglect of the local field effects, where the former and the latter tend to increase and decrease the static electronic dielectric constants [51,62,73,76]. A wider band-gap material tends to show a smaller static electronic dielectric constant associated with the weaker screening effects, and this results in a larger contribution of the non-local Fock exchange, the

TABLE II. Electronic contribution to the spherically averaged dielectric constant of group-III oxides obtained by using PBEsol and the RPA. Experimental values from Refs. [80,97,98] are shown in parentheses.

	Al_2O_3	Ga_2O_3	In_2O_3	Sc_2O_3	Y_2O_3	La_2O_3
Corundum	3.10(3.06 [97])	4.18(3.80)	4.72	4.65	4.01	4.29
β-Gallia	3.03	3.93(3.57 [80])				
κ-Alumina	3.02	3.98	4.76			
Bixbyite	3.08	4.08	4.50(4.0 [98])	4.49	3.88	4.04

TABLE III. Band gaps from non-self-consistent dielectric-dependent hybrid functional calculations compared with experimental values (in eV). No direct band gap is given if it is the same as the minimum gap in the direct-type band structure. Experimental values are from Refs. [19,24,29,34,80,99–107].

Composition	Structure	Minimum band gap	Direct band gap	Experiment
Al_2O_3	Corundum	9.44		8.8 [99], 9.5 [100]
	β-Gallia	8.01	8.31	7.4 [101]
	κ-Alumina	8.47		
	Bixbyite	8.68	8.72	
Ga_2O_3	Corundum	5.02	5.26	4.98 [102], 5.3 [19], 5.61 [29]
	β-Gallia	4.79		4.7 [80], 4.9
	κ-Alumina	4.84	4.84	4.9 [24]
	Bixbyite	4.79	4.91	
In_2O_3	Corundum	2.94	2.95	3.02 ± 0.15 [103]
	κ-Alumina	2.73	2.73	
	Bixbyite	2.91	2.91	2.9 [34]
Sc_2O_3	Corundum	6.67	6.84	
	Bixbyite	6.41		5.9 [104], 6.0 [100], 6.0-6.1 [105]
Y_2O_3	Corundum	6.88	6.99	
	Bixbyite	6.57	6.60	5.7 ± 0.1 [106], 5.7 [107], 6.2 [100]
La_2O_3	Corundum	5.93	6.25	
	Bixbyite	5.74	5.91	

amount of which is given by the reciprocal of the average of a static electronic dielectric constant in the dd hybrid functional. Here, a dielectric constant of 4 corresponds to 25% nonlocal exchange mixing that is employed in the PBE0 full-range hybrid functional [77–79], as well as the HSE06 range-separated hybrid functional [59–61].

Table III shows the minimum and direct band gaps obtained from nsc-dd hybrid functional calculations by using

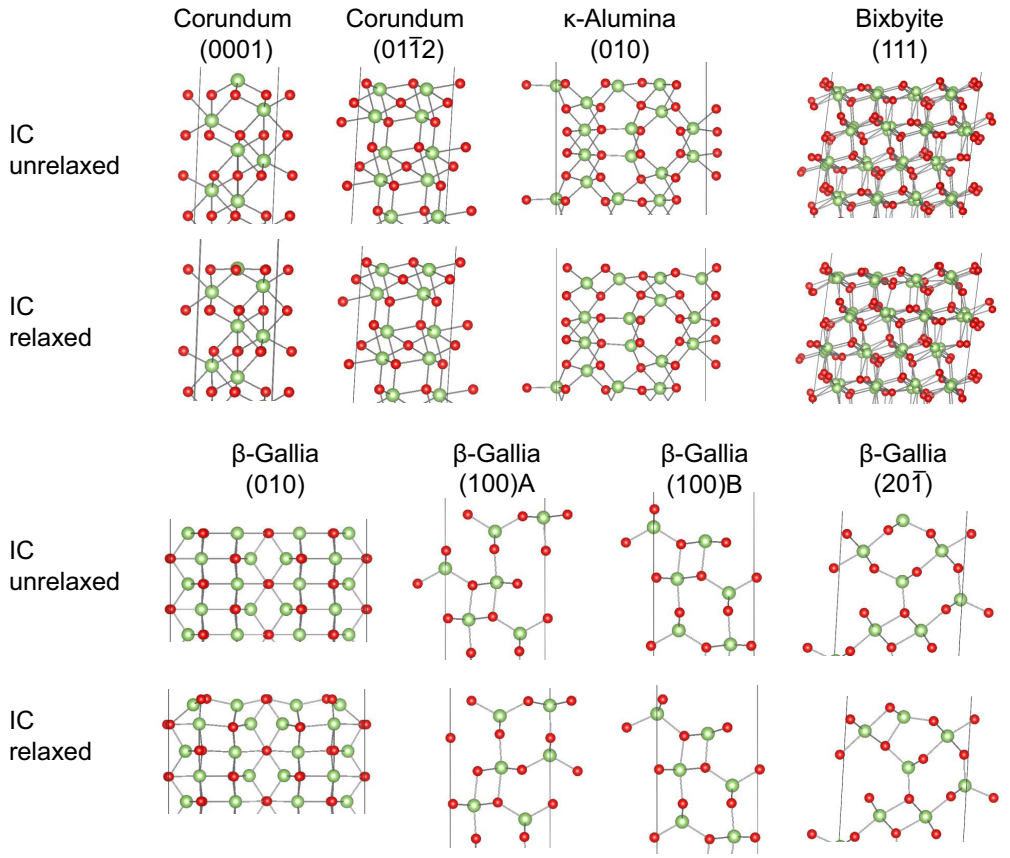

FIG. 3. Cross-sectional views of Ga_2O_3 surfaces considered for band alignment evaluation. Unrelaxed and relaxed denote structures before and after internal coordinate relaxation, respectively. Green and red balls indicate Ga and O ions, respectively. The upper edges correspond to surface planes and the black lines denote periodicity units in the directions parallel to the surface planes.

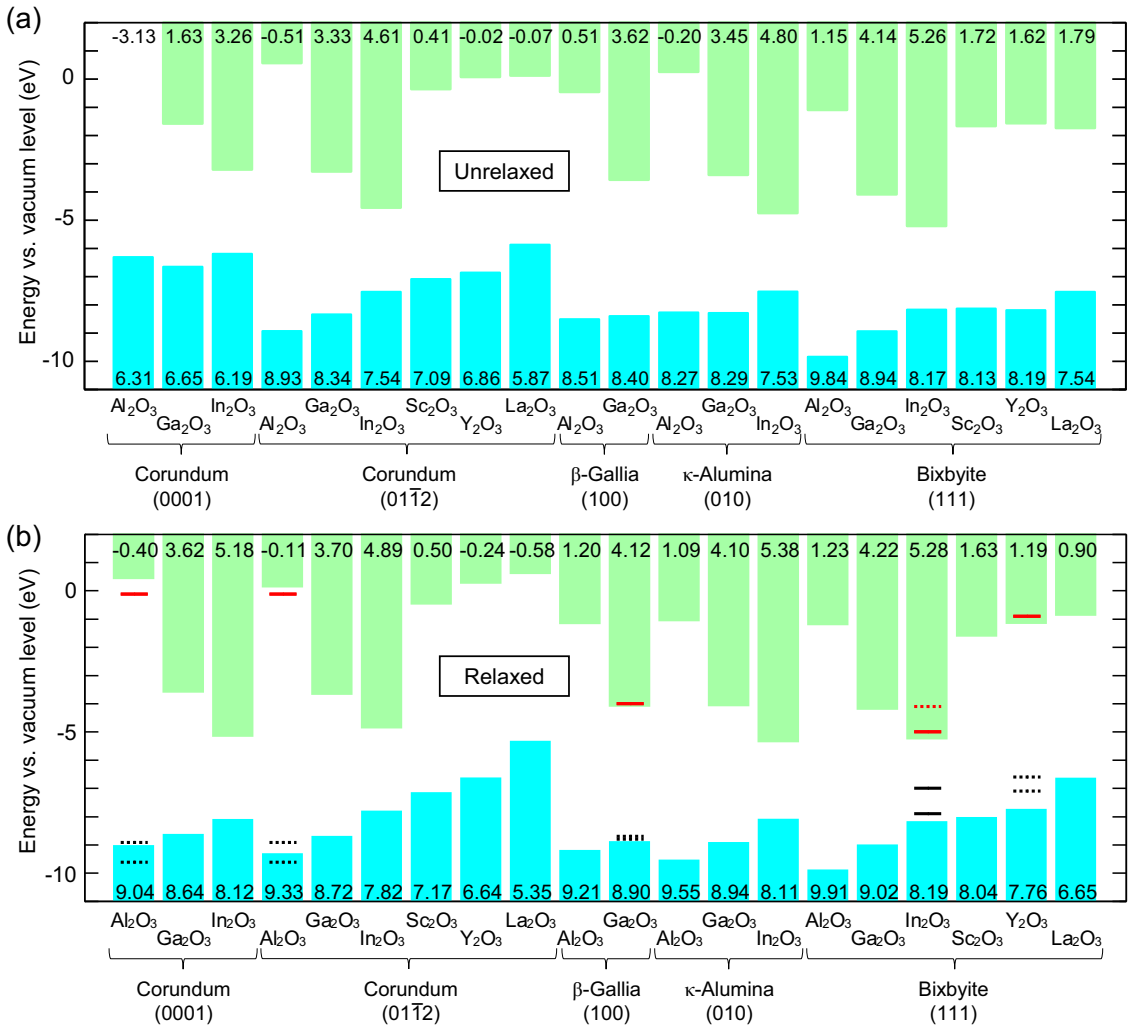

FIG. 4. VBM and CBM with respect to the vacuum level (the negatives of the IP and EA, respectively) for nonpolar surfaces of group-III oxide polymorphs obtained from non-self-consistent dielectric-dependent hybrid functional calculations; the IP and EA values are indicated at the bottom and top of the figure, respectively. Relaxation of atomic positions, i.e., internal coordinates, is (a) not taken and (b) taken into account in surface calculations. The black and red solid lines indicate experimental IP and EA values, respectively: data are from Refs. [89], [92], [36,85], and [91] for Al_2O_3, Ga_2O_3, In_2O_3, and Y_2O_3, respectively. The dotted lines are derived by combining experimentally reported IPs or EAs and the band gaps listed in Table III.

PBEsol optimized geometries. Available experimental values are shown as well. For most systems, the nsc-dd hybrid functional results are close to the experimental values although the latter shows spread for some phases. It is noted that PBEsol severely underestimates band gaps, for instance, to be 2.22 eV for Ga_2O_3 in the β-gallia structure, for which an experimental band gap of 4.7–4.9 eV [80] is relatively well established among the systems considered. The nsc-dd hybrid functional approach thus shows a significant improvement over PBEsol in the estimation of the band gaps and such improvements have also been found for group-IV, III-V, and II-VI semiconductors [62] and group-II oxides [51]. β-Ga_2O_3 shows a direct-type band structure both in our nsc-dd hybrid functional and previously reported G_0W_0@HSE03 results [81], while slightly indirect in our PBEsol result and previous reports using a tuned HSE hybrid functional [82,83]. In any case, the differences between the direct and indirect gaps are small, at most 40 meV. The reported G_0W_0@HSE03 values for the indirect and direct band gaps of α-Ga_2O_3 are 5.39 and 5.63 eV, respectively, while the direct gap of β-Ga_2O_3 is 5.05 eV [81]. These quasiparticle gaps by G_0W_0 are consistently slightly larger than our results of the nsc-dd hybrid calculations by about 0.2–0.4 eV.

B. Surface energetics and band positions

Nonpolar surfaces with low surface energies were selected for IP and EA evaluation through systematic calculations, where a total of 24 surfaces with low Miller indices and small unit surface area were considered for each chemical composition. The orientations considered are (110) and (111) for bixbyite (two terminations each); (0001), (10$\bar{1}$1), (01$\bar{1}$2), (10$\bar{1}$4), and (2$\bar{1}$ $\bar{1}$0) for corundum [(111), (100), (110), (211), and (1$\bar{1}$0) in the rhombohedral setting, respectively]; (001), (010), (100), (110), (20$\bar{1}$), and (201) for the β-gallia structure [two terminations each except for (010)]; and (010) and (100)

TABLE IV. Surface energies with natural lattice parameters with unrelaxed and relaxed internal coordinates obtained by using PBEsol for models used in band-offset calculations.

Structure	Composition	Surface plane	Surface energy (meV/Å^2) Unrelaxed	Relaxed
Corundum	Al_2O_3	(0001)	221	99
Corundum	Al_2O_3	$(01\bar{1}2)$	131	99
Corundum	Ga_2O_3	(0001)	145	59
Corundum	Ga_2O_3	$(01\bar{1}2)$	104	76
Corundum	In_2O_3	(0001)	118	68
Corundum	In_2O_3	$(01\bar{1}2)$	81	67
β-Gallia	Al_2O_3	(010)	193	139
β-Gallia	Al_2O_3	(100)A	46	28
β-Gallia	Al_2O_3	(100)B	105	66
β-Gallia	Al_2O_3	$(20\bar{1})$	184	65
β-Gallia	Ga_2O_3	(010)	139	93
β-Gallia	Ga_2O_3	(100)A	38	24
β-Gallia	Ga_2O_3	(100)B	80	50
β-Gallia	Ga_2O_3	$(20\bar{1})$	135	47

for the κ-alumina structure (two terminations each). The lowest-energy surfaces were chosen among the orientations with small in-plane area.

Figure 3 shows eight representative surfaces of Ga_2O_3 that were selected from this screening process, which are corundum (0001) and $(01\bar{1}2)$; κ-alumina (010); bixbyite (111); and β-gallia (010), $(20\bar{1})$, and (100) with two kinds of termination planes (A and B). Surfaces with and without internal coordinate relaxation are given. All of the surfaces considered in the screening except β-gallia (010) are of Tasker's type 2 [47] or type B in Hinuma *et al.* [75], and did not show substantial reconstruction of bonding by geometry optimization in all of Al_2O_3, Ga_2O_3, and In_2O_3; the β-gallia (010) surface is type 1 and type A in these definitions, respectively. For bixbyite In_2O_3, the (111) surface has been reported to be more stable than the (110), (211), and (100) with PBE-GGA [84], the local density approximation [84,85], and the HSE06 hybrid functional [86]. Our results show that the bixbyite In_2O_3 (111) surface is more stable than the (110) surface, which is consistent with these reported results.

Figure 4 shows the VBM and CBM with respect to the vacuum level (the negatives of the IP and EA, respectively) obtained by using nsc-dd hybrid functional calculations. The most stable surface after internal coordinate relaxation is considered for each compound, except for corundum Al_2O_3, Ga_2O_3, and In_2O_3 where both (0001) and $(01\bar{1}2)$ surfaces are shown because the surface energy is almost the same; the surface energies after relaxation for the two corundum (0001) and $(01\bar{1}2)$ surfaces are almost the same within a few meV/Å^2 in Al_2O_3 and In_2O_3, while $(01\bar{1}2)$ is slightly less stable in Ga_2O_3 (Table IV). Results both with and without internal coordinate relaxation are shown, and the former is compared with available experimental values in Fig. 4(b). Exactly speaking, IPs and EAs are dependent on the surface composition and atomistic structure and, therefore, the comparison between theory and experiment should be made for identical surfaces [87]. Unlike prototypical zinc-blende and wurtzite semiconductors [88], the experimental reports on the IPs and EAs for group-III oxide surfaces with orientations and detailed atomistic structures specified are limited. Therefore, we include the experimental values in Fig. 4(b) that are measured for different or unspecified surface orientations [89–91] and estimated from Au/β-Ga_2O_3 (100) [92], Al/Y_2O_3, Ag/Y_2O_3, and Ni/Y_2O_3 Schottky junctions [91]. Nevertheless, such a comparison would be meaningful given that the chemical composition and crystal structure are important factors to determine the band position [51]. Moreover, when only either of the IP or EA has been reported experimentally, we estimate the other value by using an experimental band gap. This causes an ambiguity when reported values for experimental band gaps show some spread (Table III). On this basis, a reasonable agreement between theory and experiment is found in Fig. 4(b), which would indicate the effectiveness of the present nsc-dd hybrid functional approach for the prediction of the surface band positions of group-III oxides, as well as those of prototypical semiconductors [62,73] and group-II oxides [51]; the experimental IP of In_2O_3 was reported to be 7.0 eV for the (111) surface of a film on Y-stabilized ZrO_2 and 7.7 eV for an oxidized polar (100) surface [85], and our result on a stoichiometric surface is closer to the latter value. In addition, similar theoretical VBM positions of the Ga_2O_3 polymorphs against the vacuum level are consistent with recent reports by Peelaers *et al.* [31] and by Lyons [93] using the HSE functional with a tuned Fock-exchange mixing value of 0.32, although the surface orientations are different between their studies and ours.

A chemical tendency is recognized in the band positions, particularly when compared within the same crystal structures and surface planes. The IP tends to decrease (the VBM increases) as the cation goes down the periodic table for all surfaces within the same crystal structure and surface plane. This trend is much clearer for the relaxed surfaces shown in Fig. 4(b). To make this observation more evident, Figs. 5(a)–5(c) show the VBM plotted against the reciprocal of the cube root of volume per atom before and after internal coordinate relaxation, and their differences, respectively. The VBM for each surface orientation decreases with increasing reciprocal of the cube root of volume per atom, which is a trend also found in group-II oxides and explainable in terms of the common O-2p valence-band component and the Madelung potential [51]. However, the trend is not monotonic because the VBM of Sc_2O_3 is higher than In_2O_3 even though the former has a smaller volume per atom. This implies that the volume per atom is a significant contributor but not the single determinant of the VBM order. Cation electronegativity is not a good reason because the Pauling electronegativity decreases as the cation goes down the periodic table in group IIIA from 1.3 in Sc to 1.1 in La but increases in group IIIB from 1.5 in Al to 1.7 in In.

Relaxation of ICs in slab calculations tends to shift the VBM downward from the vacuum level (increase the IP) when the constituent cation is lighter and/or smaller in ionic size, and vice versa, as evident in Fig. 5(c). A similar trend was found in nonpolar type A (Tasker's type 1) surfaces of group-II oxides in Ref. [51]. Smaller cations tend to relax toward the bulk side compared with O ions, while larger cations tend to relax toward the vacuum side, enhancing the magnitude of surface dipoles of opposite sign [51,94]. As

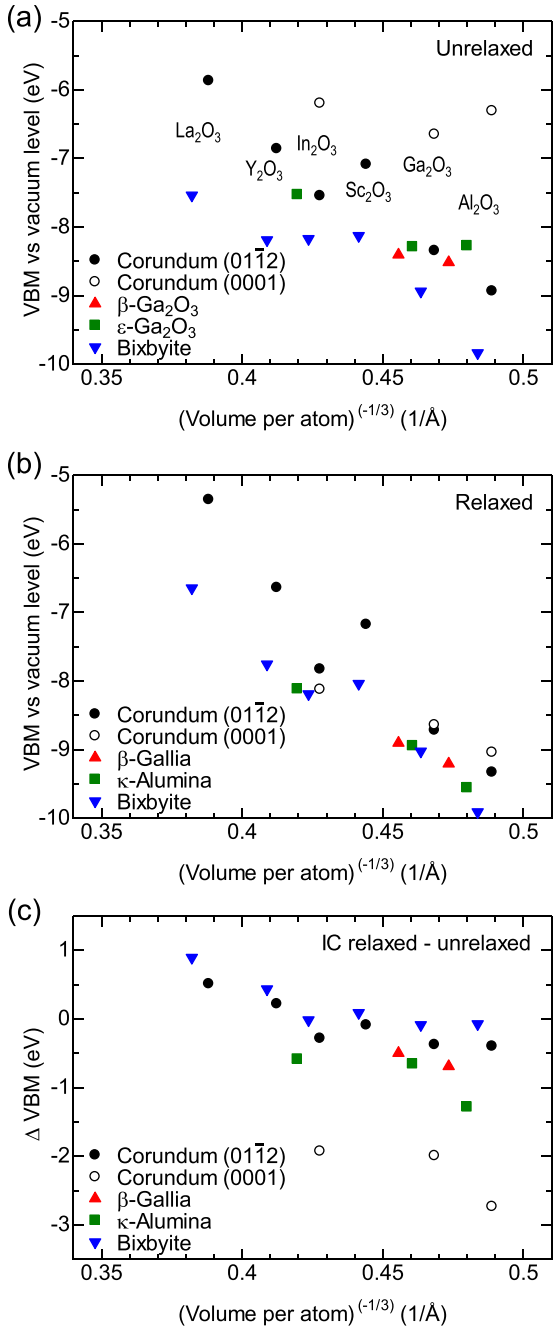

FIG. 5. VBM with respect to the vacuum level (the negative of the IP) when the internal coordinates in slab calculations are (a) unrelaxed and (b) relaxed, and (c) difference between the unrelaxed and relaxed values in panels (a) and (b). Values are from non-self-consistent dielectric-dependent hybrid functional calculations.

a result, the tendency that oxides for smaller cations have lower VBMs (large IPs) becomes clearer. The amount of the VBM shift strongly depends on the surface orientation. In particular, the corundum (0001) surfaces for Al_2O_3, Ga_2O_3, and In_2O_3 generally exhibit noticeable relaxation effects of as large as or even larger than 2 eV. These surfaces have cations on the outmost layer and they relax substantially toward the bulk region, as shown for the case of Ga_2O_3 in Fig. 3. Such huge relaxation would largely modify the surface dipoles and thereby the band positions.

TABLE V. Natural valence-band offsets at Al_2O_3/Ga_2O_3 interfaces obtained from non-self-consistent dielectric-dependent hybrid functional calculations. The ionization potential (IP) differences for the corresponding relaxed and unrelaxed surfaces are compared. Positive and negative values mean that the VBM of Al_2O_3 is higher and lower than that of Ga_2O_3, respectively.

	Interfacial valence-band	IP difference	
Interface	offset	Relaxed	Unrelaxed
Corundum (0001)	0.04	−0.39	0.34
Corundum (01$\bar{1}$2)	−0.75	−0.61	−0.59
β-Gallia (010)	0.05	−0.16	0.18
β-Gallia (100)A	−0.14	−0.29	−0.10
β-Gallia (100)B	−0.76	−0.89	−0.84
β-Gallia (20$\bar{1}$)	−0.29	−0.56	−0.20

C. Interfacial band offsets

In this section, we discuss valence-band offsets at heterointerfaces with an emphasis on the comparison between the offset values obtained by using interfacial models and the surface IP differences; a similar discussion holds for the interfacial conduction-band offsets and the surface EA differences. Table V shows the natural (unstrained) valence-band offsets of Al_2O_3 versus Ga_2O_3 obtained by using the procedures described in Sec. II B. The natural interfacial offset evaluation involves strained and unstrained surface terms in Eq. (1) to consider the effects of strain relief. Here, the bulk values are used for "IC" in these terms. We found that the differences are only within 0.2 eV when the relaxed internal coordinates are used instead, except for the β-gallia (010) and (20$\bar{1}$) Al_2O_3/Ga_2O_3 interfaces with differences of 0.35 and 0.41 eV, respectively. A large discrepancy between the two IC cases is possible when there is significant internal coordinate relaxation in the surface model and when the amount of relaxation, and therefore the magnitude of the surface dipole, depends largely on the lattice constants. Indeed, the β-gallia (20$\bar{1}$) Al_2O_3 and Ga_2O_3 surfaces do relax significantly; relaxation changes the outermost layer from a cation layer to an O ion layer. However, excessive relaxation cannot always be identified by simple visual inspection. For example, the relaxation at the β-gallia (010) Al_2O_3 and Ga_2O_3 surface is not as extreme (see Fig. 3 for the case of Ga_2O_3). The energies of the (010) and (20$\bar{1}$) surfaces of β-gallia Al_2O_3 and Ga_2O_3 with fixed internal coordinates are ∼4 times higher than the minimum surface energy (Table IV), which is of the (100)A surface. We base the following discussion on the interfacial offset results with unrelaxed (bulk) internal coordinates because such large strain-dependent relaxation effects should be avoided as much as possible.

Turning to the IP difference, it is significantly affected by internal coordinate relaxation effects for corundum (0001) as well as β-gallia (010) and (20$\bar{1}$) Al_2O_3/Ga_2O_3: $|\Delta\varepsilon^{\mathrm{A-B}}_{\mathrm{Surface,Natural,Relaxed}} - \Delta\varepsilon^{\mathrm{A-B}}_{\mathrm{Surface,Natural,Bulk}}| = 0.73,\ 0.34,$ and 0.36 eV, respectively, as shown in Table V. Internal coordinate relaxation also strongly impacts the interfacial band offset in the latter two pairs as mentioned above. The corundum (0001) surface is subject to extensive relaxation of internal coordinates (see Fig. 3 for the case of Ga_2O_3),

TABLE VI. Strain in the in-plane lattice parameters a and b of coherent Al_2O_3/Ga_2O_3 heterointerface models.

	Al_2O_3		Ga_2O_3	
Interface	a	b	a	b
Corundum (0001)	2.4%	2.4%	−2.3%	−2.3%
Corundum (01$\bar{1}$2)	2.1%	1.7%	−2.6%	−2.1%
β-Gallia (010)	1.5%	1.8%	−1.6%	−2.1%
β-Gallia (100)A	2.2%	1.5%	−2.2%	−1.6%
β-Gallia (100)B	2.1%	1.5%	−2.2%	−1.6%
β-Gallia (20$\bar{1}$)	2.2%	1.8%	−2.1%	−2.1%

and the reduction in surface energy with relaxation is much larger than the (01$\bar{1}$2) surface (Table IV). In other cases, the choice of whether to relax internal coordinates does not make a significant change in the derived IP difference. The use of the IP difference without internal coordinate relaxation in the surface calculations would be more reasonable for the purpose of interfacial offset estimation because the relaxation at the interface is restricted by the presence of the counterpart material.

Comparing the interfacial band offsets and the IP differences for unrelaxed surfaces in Table V, $|\Delta\varepsilon^{A-B}_{Interface,Natural,Bulk} - \Delta\varepsilon^{A-B}_{Surface,Natural,Bulk}|$ are at most 0.3 eV for all Al_2O_3/Ga_2O_3 systems. The IP differences without surface internal coordinate relaxation indeed provide reasonable estimates of valence-band offsets at these interfaces with relatively small lattice misfits of a few percent in the in-plane directions (Table VI). In contrast, we found that $|\Delta\varepsilon^{A-B}_{Interface,Natural,Bulk} - \Delta\varepsilon^{A-B}_{Surface,Natural,Bulk}|$ is much larger, for instance, for In_2O_3/Ga_2O_3 with larger lattice misfits of ∼10%: 1.23 and 0.81 eV for corundum (0001) and (01$\bar{1}$2), respectively. Accurate prediction of the natural band offsets would be challenging with such large misfits because the coherent interface model with significant strain may not be appropriate. Relevant to this issue, our previous study investigating the effects of misfit dislocations at zincblende CdTe/CdS, CdS/ZnS, and InP/GaP (110) interfaces with 7%–10% misfits indicates that an explicit consideration of misfit dislocations changes potential offsets typically by only 0.1 eV or less at a distance of ∼1 nm from the dislocations [95]. In other words, the strained interface models without misfit dislocations work well for estimating interfacial offsets. Such strain effects could, however, be different for corundum In_2O_3/Ga_2O_3 with a more complicated structure.

There are significant orientation and/or termination dependencies of the interfacial offsets within the same interface composition and crystal structure. We found that this is not necessarily related to the interfacial energies. For instance, the β-gallia (100)A and (100)B Al_2O_3/Ga_2O_3 interfaces show an offset difference of ∼0.6 eV, but their interfacial energies are almost identical within ∼0.01 meV Å^{-2} (0.1 mJ m^{-2}). Peelaers *et al.* estimated the valence-band offsets at corundum (10$\bar{1}$0) and β-gallia (010) Al_2O_3/Ga_2O_3 interfaces to be −0.24 and 0.37 eV, respectively, where the negative (positive) value indicates the VBM of Al_2O_3 is lower (higher) than that of Ga_2O_3, along with the band positions of $(Al_xGa_{1-x})_2O_3$ alloys via IP difference calculations using the HSE hybrid functional with a tuned Fock-exchange mixing value of 0.32 [31]. Wang *et al.* gave values of −0.11 and 0.33 eV, respectively, for these two interfaces via explicit interface calculations using HSE with 0.32 mixing [30]. The discrepancies between our results and Refs. [30,31] for β-gallia (010) Al_2O_3/Ga_2O_3 may be attributed to the difference in the functional form and parameter values that yields a band-gap difference of ∼0.1 eV for Al_2O_3 and the derivation procedure for IP differences and interfacial natural band offsets: the Fock-exchange mixing values are 0.33 and 0.25 for Al_2O_3 and Ga_2O_3 in the β-gallia structure, respectively, in our study using a dd full-range hybrid functional, while a range-separated HSE functional was used in Refs. [30,31] with the aforementioned Fock-exchange mixing value of 0.32 and a screening parameter.

IV. CONCLUSIONS

The band alignments at nonpolar surfaces and heterointerfaces of group-III oxides were investigated by using nsc-dd hybrid functional calculations. The lowest-energy phases are corundum, β-gallia, A-type rare earth, and bixbyite for Al_2O_3, Ga_2O_3, La_2O_3, and the others, respectively, within PBEsol calculations. The IP typically decreases (the VBM increases) in the order Al_2O_3, Ga_2O_3, In_2O_3, Sc_2O_3, Y_2O_3, and La_2O_3 within the same crystal structure and surface termination, indicating that a smaller cation results in a larger IP (a lower VBM). This tendency is enhanced by the atomic relaxation-induced surface dipoles, where smaller cations tend to relax toward the bulk side compared to O ions, while larger cations tend to relax toward the vacuum side. Comparison of the band offset for Al_2O_3/Ga_2O_3 calculated with and without an explicit interface model suggested that the IP (EA) difference at unrelaxed surfaces is a good indicator of the interfacial valence (conduction) band offset.

ACKNOWLEDGMENTS

This study was supported by the "Materials Research by Information Integration" Initiative (MI^{2}I) project of the Support Program for Starting Up Innovation Hub as well as CREST (Grants No. JPMJCR17J2 and No. JPMJCR17J3) from the Japan Science and Technology Agency (JST), and by a Grant-in-Aid for Scientific Research (C) (No. 18K04692) from the Japan Society for the Promotion of Science (JSPS). Computing resources of the Research Institute for Information Technology at Kyushu University, ACCMS at Kyoto University, and the Supercomputer Center in the Institute for Solid State Physics at the University of Tokyo were used. The VESTA code [96] was used to draw Figs. 1 and 3.

[1] F. A. Ponce and D. P. Bour, Nature (London) **386**, 351 (1997).

[2] B. J. H. Stadler, M. Oliveria, and L. O. Bouthillette, J. Am. Ceram. Soc. **78**, 3336 (1995).

[3] G. D. Wilk, R. M. Wallace, and J. M. Anthony, J. Appl. Phys. **89**, 5243 (2001).
[4] A. H. Heuer, D. B. Hovis, J. L. Smialek, and B. Gleeson, J. Am. Ceram. Soc. **94**, s146 (2011).
[5] K. Shirvani, S. Mastali, A. Rashidghamat, and H. Abdollahpour, Corros. Sci. **75**, 142 (2013).
[6] A. Aiello, A. Ciampichetti, and G. Benamati, J. Nucl. Mater. **329–333**, 1398 (2004).
[7] M. Moses-DeBusk, M. Yoon, L. F. Allard, D. R. Mullins, Z. Wu, X. Yang, G. Veith, G. M. Stocks, and C. K. Narula, J. Am. Chem. Soc. **135**, 12634 (2013).
[8] C. K. Narula, L. F. Allard, G. M. Stocks, and M. Moses-DeBusk, Sci. Rep. **4**, 7238 (2014).
[9] T. Oshima, T. Okuno, N. Arai, N. Suzuki, S. Ohira, and S. Fujita, Appl. Phys. Express **1**, 011202 (2008).
[10] D. Y. Guo, Z. P. Wu, Y. H. An, X. C. Guo, X. L. Chu, C. L. Sun, L. H. Li, P. G. Li, and W. H. Tang, Appl. Phys. Lett. **105**, 023507 (2014).
[11] M. Fleischer, L. Höllbauer, and H. Meixner, Sens. Actuator B-Chem. **18**, 119 (1994).
[12] N. Ueda, H. Hosono, R. Waseda, and H. Kawazoe, Appl. Phys. Lett. **70**, 3561 (1997).
[13] M. Orita, H. Ohta, M. Hirano, and H. Hosono, Appl. Phys. Lett. **77**, 4166 (2000).
[14] M. Higashiwaki, K. Sasaki, H. Murakami, Y. Kumagai, A. Koukitu, A. Kuramata, T. Masui, and S. Yamakoshi, Semicond. Sci. Technol. **31**, 034001 (2016).
[15] M. A. Mastro, A. Kuramata, J. Calkins, J. Kim, F. Ren, and S. J. Pearton, ECS J. Solid State Sci. Technol. **6**, P356 (2017).
[16] I. Cora, F. Mezzadri, F. Boschi, M. Bosi, M. Čaplovičová, G. Calestani, I. Dódony, B. Pécz, and R. Fornari, CrystEngComm **19**, 1509 (2017).
[17] S. Yoshioka, H. Hayashi, A. Kuwabara, F. Oba, K. Matsunaga, and I. Tanaka, J. Phys.: Condens. Matter **19**, 346211 (2007).
[18] M. B. Maccioni and V. Fiorentini, Appl. Phys. Express **9**, 041102 (2016).
[19] D. Shinohara and S. Fujita, Jpn. J. Appl. Phys. **47**, 7311 (2008).
[20] D. Y. Guo, X. L. Zhao, Y. S. Zhi, W. Cui, Y. Q. Huang, Y. H. An, P. G. Li, Z. P. Wu, and W. H. Tang, Mater. Lett. **164**, 364 (2016).
[21] H. Hayashi, R. Huang, H. Ikeno, F. Oba, S. Yoshioka, I. Tanaka, and S. Sonoda, Appl. Phys. Lett. **89**, 181903 (2006).
[22] H. Hayashi, R. Huang, F. Oba, T. Hirayama, and I. Tanaka, J. Mater. Res. **26**, 578 (2011).
[23] T. Oshima, K. Matsuyama, K. Yoshimatsu, and A. Ohtomo, J. Cryst. Growth **421**, 23 (2015).
[24] Y. Oshima, E. G. Víllora, Y. Matsushita, S. Yamamoto, and K. Shimamura, J. Appl. Phys. **118**, 085301 (2015).
[25] F. Boschi, M. Bosi, T. Berzina, E. Buffagni, C. Ferrari, and R. Fornari, J. Cryst. Growth **443**, 25 (2016).
[26] X. Xia, Y. Chen, Q. Feng, H. Liang, P. Tao, M. Xu, and G. Du, Appl. Phys. Lett. **108**, 202103 (2016).
[27] E. Chikoidze, H. J. v. Bardeleben, K. Akaiwa, E. Shigematsu, K. Kaneko, S. Fujita, and Y. Dumont, J. Appl. Phys. **120**, 025109 (2016).
[28] N. Suzuki, S. Ohira, M. Tanaka, T. Sugawara, K. Nakajima, and T. Shishido, Phys. Status Solidi C **4**, 2310 (2007).
[29] H. Ito, K. Kaneko, and S. Fujita, Jpn. J. Appl. Phys. **51**, 100207 (2012).
[30] T. Wang, W. Li, C. Ni, and A. Janotti, Phys. Rev. Appl. **10**, 011003 (2018).
[31] H. Peelaers, J. B. Varley, J. S. Speck, and C. G. V. d. Walle, Appl. Phys. Lett. **112**, 242101 (2018).
[32] I. Hamberg and C. G. Granqvist, J. Appl. Phys. **60**, R123 (1986).
[33] C. G. Granqvist and A. Hultåker, Thin Solid Films **411**, 1 (2002).
[34] A. Walsh, J. L. F. Da Silva, S.-H. Wei, C. Körber, A. Klein, L. F. J. Piper, A. DeMasi, K. E. Smith, G. Panaccione, P. Torelli, D. J. Payne, A. Bourlange, and R. G. Egdell, Phys. Rev. Lett. **100**, 167402 (2008).
[35] D. Cahen and A. Kahn, Adv. Mater. **15**, 271 (2003).
[36] H. Hosono, *Transparent Electronics: From Synthesis to Applications* (Wiley, New York, 2010).
[37] A. Franciosi and C. G. Van de Walle, Surf. Sci. Rep. **25**, 1 (1996).
[38] J. Robertson, J. Vac. Sci. Technol. A **31**, 050821 (2013).
[39] E. T. Yu, J. O. McCaldin, and T. C. McGill, in *Solid State Physics*, edited by E. Henry and T. David (Academic Press, Boston, 1992), p. 1.
[40] Y. Hinuma, A. Grüneis, G. Kresse, and F. Oba, Phys. Rev. B **90**, 155405 (2014).
[41] Y. Hinuma, F. Oba, Y. Kumagai, and I. Tanaka, Phys. Rev. B **88**, 035305 (2013).
[42] Y. Hinuma, F. Oba, Y. Nose, and I. Tanaka, J. Appl. Phys. **114**, 043718 (2013).
[43] R. L. Anderson, Solid·State Electron. **5**, 341 (1962).
[44] Y. Guo, H. Li, S. J. Clark, and J. Robertson, J. Phys. Chem. C **123**, 5562 (2019).
[45] Y. Ping, D. Rocca, and G. Galli, Chem. Soc. Rev. **42**, 2437 (2013).
[46] Y. Kumagai, K. T. Butler, A. Walsh, and F. Oba, Phys. Rev. B **95**, 125309 (2017).
[47] P. W. Tasker, J. Phys. C: Solid State Phys. **12**, 4977 (1979).
[48] A. Alkauskas and A. Pasquarello, Physica B: Condensed Matter **401–402**, 670 (2007).
[49] F. Tran, Phys. Lett. A **376**, 879 (2012).
[50] D. Koller, P. Blaha, and F. Tran, J. Phys.: Condens. Matter **25**, 435503 (2013).
[51] Y. Hinuma, Y. Kumagai, I. Tanaka, and F. Oba, Phys. Rev. Mater. **2**, 124603 (2018).
[52] P. E. Blöchl, Phys. Rev. B **50**, 17953 (1994).
[53] G. Kresse and J. Furthmüller, Phys. Rev. B **54**, 11169 (1996).
[54] G. Kresse and D. Joubert, Phys. Rev. B **59**, 1758 (1999).
[55] J. P. Perdew, A. Ruzsinszky, G. I. Csonka, O. A. Vydrov, G. E. Scuseria, L. A. Constantin, X. Zhou, and K. Burke, Phys. Rev. Lett. **100**, 136406 (2008).
[56] J. P. Perdew, K. Burke, and M. Ernzerhof, Phys. Rev. Lett. **77**, 3865 (1996).
[57] Y. Hinuma, H. Hayashi, Y. Kumagai, I. Tanaka, and F. Oba, Phys. Rev. B **96**, 094102 (2017).
[58] J. Sun, A. Ruzsinszky, and J. P. Perdew, Phys. Rev. Lett. **115**, 036402 (2015).
[59] J. Heyd, G. Scuseria, and M. Ernzerhof, J. Chem. Phys. **118**, 8207 (2003).
[60] J. Heyd, G. E. Scuseria, and M. Ernzerhof, J. Chem. Phys. **124**, 219906 (2006).
[61] A. V. Krukau, O. A. Vydrov, A. F. Izmaylov, and G. E. Scuseria, J. Chem. Phys. **125**, 224106 (2006).

[62] Y. Hinuma, Y. Kumagai, I. Tanaka, and F. Oba, Phys. Rev. B **95**, 075302 (2017).

[63] T. Shimazaki and Y. Asai, Chem. Phys. Lett. **466**, 91 (2008).

[64] M. A. L. Marques, J. Vidal, M. J. T. Oliveira, L. Reining, and S. Botti, Phys. Rev. B **83**, 035119 (2011).

[65] M. Gerosa, C. E. Bottani, L. Caramella, G. Onida, C. Di Valentin, and G. Pacchioni, Phys. Rev. B **91**, 155201 (2015).

[66] J. H. Skone, M. Govoni, and G. Galli, Phys. Rev. B **89**, 195112 (2014).

[67] T. Shimazaki and T. Nakajima, J. Chem. Phys. **141**, 114109 (2014).

[68] J. H. Skone, M. Govoni, and G. Galli, Phys. Rev. B **93**, 235106 (2016).

[69] M. Gerosa, C. E. Bottani, C. D. Valentin, G. Onida, and G. Pacchioni, J. Phys.: Condens. Matter **30**, 044003 (2018).

[70] W. Chen, G. Miceli, G.-M. Rignanese, and A. Pasquarello, Phys. Rev. Mater. **2**, 073803 (2018).

[71] S. Baroni and R. Resta, Phys. Rev. B **33**, 7017 (1986).

[72] M. Gajdoš, K. Hummer, G. Kresse, J. Furthmüller, and F. Bechstedt, Phys. Rev. B **73**, 045112 (2006).

[73] F. Oba and Y. Kumagai, Appl. Phys. Express **11**, 060101 (2018).

[74] Y. Hinuma, T. Hatakeyama, Y. Kumagai, L. A. Burton, H. Sato, Y. Muraba, S. Iimura, H. Hiramatsu, I. Tanaka, H. Hosono, and F. Oba, Nat. Commun. **7**, 11962 (2016).

[75] Y. Hinuma, Y. Kumagai, F. Oba, and I. Tanaka, Comp. Mater. Sci. **113**, 221 (2016).

[76] M. Shishkin, M. Marsman, and G. Kresse, Phys. Rev. Lett. **99**, 246403 (2007).

[77] J. Perdew, M. Ernzerhof, and K. Burke, J. Chem. Phys. **105**, 9982 (1996).

[78] C. Adamo and V. Barone, J. Chem. Phys. **110**, 6158 (1999).

[79] M. Ernzerhof and G. Scuseria, J. Chem. Phys. **110**, 5029 (1999).

[80] M. Rebien, W. Henrion, M. Hong, J. P. Mannaerts, and M. Fleischer, Appl. Phys. Lett. **81**, 250 (2002).

[81] J. Furthmüller and F. Bechstedt, Phys. Rev. B **93**, 115204 (2016).

[82] H. Peelaers and C. G. Van de Walle, Phys. Status Solidi B **252**, 828 (2015).

[83] T. Gake, Y. Kumagai, and F. Oba, Phys. Rev. Mater. **3**, 044603 (2019).

[84] P. Agoston and K. Albe, Phys. Rev. B **84**, 045311 (2011).

[85] M. V. Hohmann, P. Ágoston, A. Wachau, T. J. M. Bayer, J. Brötz, K. Albe, and A. Klein, J. Phys.: Condens. Matter **23**, 334203 (2011).

[86] A. Walsh and C. R. A. Catlow, J. Mater. Chem. **20**, 10438 (2010).

[87] A. Grüneis, G. Kresse, Y. Hinuma, and F. Oba, Phys. Rev. Lett. **112**, 096401 (2014).

[88] W. Mönch, in *Semiconductor Surfaces and Interfaces* (Springer, Berlin, 2001).

[89] R. Bindi, P. Iacconi, D. Lapraz, and F. Petel, J. Phys. D: Appl. Phys. **30**, 137 (1997).

[90] S. J. Pearton, C. R. Abernathy, and F. Ren, *Gallium Nitride Processing for Electronics, Sensors and Spintronics*, 1st ed. (Springer-Verlag, London, 2006).

[91] J. Y.-m. Lee and B. C. Lai, in *Ferroelectric and Dielectric Thin Films*, edited by H. S. Nalwa (Academic Press, San Diego, 2002).

[92] M. Mohamed, K. Irmscher, C. Janowitz, Z. Galazka, R. Manzke, and R. Fornari, Appl. Phys. Lett. **101**, 132106 (2012).

[93] J. L. Lyons, ECS J. Solid State Sci. Technol. **8**, Q3226 (2019).

[94] Y. Kumagai, L. A. Burton, A. Walsh, and F. Oba, Phys. Rev. Appl. **6**, 014009 (2016).

[95] Y. Hinuma, F. Oba, and I. Tanaka, Phys. Rev. B **88**, 075319 (2013).

[96] K. Momma and F. Izumi, J. Appl. Crystallogr. **44**, 1272 (2011).

[97] M. Schubert, T. E. Tiwald, and C. M. Herzinger, Phys. Rev. B **61**, 8187 (2000).

[98] M. Marezio, Acta Crystallogr. **20**, 723 (1966).

[99] R. H. French, J. Am. Ceram. Soc. **73**, 477 (1990).

[100] A. V. Emeline, G. V. Kataeva, V. K. Ryabchuk, and N. Serpone, J. Phys. Chem. B **103**, 9190 (1999).

[101] R. Franchy, G. Schmitz, P. Gassmann, and F. Bartolucci, Appl. Phys. A **65**, 551 (1997).

[102] G. Sinha, K. Adhikary, and S. Chaudhuri, J. Cryst. Growth **276**, 204 (2005).

[103] P. D. C. King, T. D. Veal, F. Fuchs, C. Y. Wang, D. J. Payne, A. Bourlange, H. Zhang, G. R. Bell, V. Cimalla, O. Ambacher, R. G. Egdell, F. Bechstedt, and C. F. McConville, Phys. Rev. B **79**, 205211 (2009).

[104] D. C. Hays, B. P. Gila, S. J. Pearton, R. Thorpe, and F. Ren, Vacuum **136**, 137 (2017).

[105] V. V. Afanas'ev, S. Shamuilia, M. Badylevich, A. Stesmans, L. F. Edge, W. Tian, D. G. Schlom, J. M. J. Lopes, M. Roeckerath, and J. Schubert, Microelectron. Eng. **84**, 2278 (2007).

[106] W. C. Wang, M. Badylevich, V. V. Afanas'ev, A. Stesmans, C. Adelmann, S. V. Elshocht, J. A. Kittl, M. Lukosius, C. Walczyk, and C. Wenger, IOP Conference Series: Materials Science and Engineering **8**, 012028 (2010).

[107] Y. Zhao, K. Kita, K. Kyuno, and A. Toriumi, Appl. Phys. Lett. **94**, 042901 (2009).